3D Roughness Prediction Modeling and Evaluation of Textured Liner of Piston Component-Cylinder System

Yanjun Lü[1,2], Cheng Liu[1,2], Yongfang Zhang[3*] , Cheng Jiang[1,2], Xudong Bai[1,2] and Zhiguo Xing[4]

Abstract

In this study, a machine vision method is proposed to characterize 3D roughness of the textured surface on cylinder liner processed by plateau honing. The least absolute value ($L\infty$) regression robust algorithm and Levenberg-Marquardt (LM) algorithm are employed to reconstruct image reference plane. On this basis, a single-hidden layer feedforward neural network (SLFNN) based on the extreme learning machine (ELM) is employed to model the relationship between high frequency information and 3D roughness. The characteristic parameters of Abbott-Firestone curve and 3D roughness measured by a confocal microscope are used to construct ELM-SLFNN prediction model for 3D roughness. The results indicate that the proposed method can effectively characterize 3D roughness of the textured surface of cylinder liner.

Keywords Surface texture, Cylinder liner, 3D roughness, Neural network

1 Introduction

With the continuous improvement of the service performance of internal combustion power equipment, the piston assembly-cylinder liner system usually conducts energy conversion and power transfer under high-speed operation. The piston assembly-cylinder liner system is subject to more complex mechanical load and thermal load under the extremely harsh working conditions [1]. The piston assembly-cylinder liner system and the interaction interface of each subsystem often exhibit complex tribological behavior, and its service performance and

efficiency directly depend on the service reliability of components such as piston assembly and cylinder liner [2]. The evolution of the service reliability of the piston assembly-cylinder liner system is closely related to the tribological behavior of the movement and the change of the machined surface topography [3, 4]. Therefore, accurate measurement and characterization of the surface topography is of great significance to the service performance of the internal combustion engines [5–9].

For the measurement of surface roughness of anti-friction texture, there are two kind of methods: contact detection and non-contact detection methods [10–16]. Compared with contact methods, non-contact methods have the advantages of low cost, high accuracy, high efficiency. Therefore, more attention have been paid to non-contact methods. Tao et al. [16] proposed a new index, i.e., undeformed chip width, to describe the stochastic characteristics in the wafer self-rotational grinding process, and used the linear regression method to obtain the roughness. Their work shows that the proposed model has high accuracy and can effectively predict the roughness of ground wafer. Lawrence et al.

*Correspondence:
Yongfang Zhang
zhangyf@xaut.edu.cn
[1] School of Mechanical and Precision Instrument Engineering, Xi'an University of Technology, Xi'an 710048, China
[2] State Key Laboratory for Manufacturing Systems Engineering, Xi'an Jiaotong University, Xi'an 710049, China
[3] School of Printing, Packaging Engineering and Digital Media Technology, Xi'an University of Technology, Xi'an 710054, China
[4] National Key Laboratory for Remanufacturing, Army Academy of Armored Forces, Beijing 100072, China

Lü *et al. Chinese Journal of Mechanical Engineering*   (2024) 37:99

Page 2 of 13

[17] used Gaussian filtering to extract the high frequency information of the surface gray image of the honing cylinder liner. BP neural network is used to obtain.

2D and 3D roughness parameters. The traditional filtering method often be lowered by the "valley" and distortion of the reference plane was not considered in their works. Samtas et al. [18] converted the grinding surface image into a binary model, and used the artificial neural network (ANN) to obtain the roughness. Their work shows that the proposed method can effectively measure the roughness characteristics of machined surfaces. Zuperl et al. [19] proposed a roughness prediction model to achieve grinding roughness by genetic algorithms (GA), artificial neural network and adaptive neural fuzzy algorithm (ANFA). The size of the virtual image area formed by color light sources on different rough surfaces is considered, and a correlation model between color image sharpness index and roughness is constructed to evaluate the roughness [20–23]. Umamaheswara Raju et al. [24] used curvelet transform to obtain the characteristic parameters of the gray image of surface topography, which realized the evaluation of 2D roughness topography. The above works [17–24] did not consider the influence of the anti-friction texture on the surface when reconstruct the reference plane of surface gray image.

In this study, a machine vision method is proposed to characterize 3D roughness of the textured surface on cylinder liner processed by plateau honing. It is necessary to consider the distortion of the reference plane caused by the surface texture, and establish the prediction model of the surface roughness characteristics based on the gray image information. According to the gray image information of the surface texture, L∞ regression robust algorithm and LM algorithm are employed to reconstruct image reference plane, which can achieve the separation of high frequency information related to roughness. On this basis, an improved ELM algorithm is employed to model the relationship between high frequency information and 3D roughness. ELM-SLFNN prediction model is constructed to evaluate 3D roughness. The proposed method can effectively characterize 3D roughness of the textured surface of cylinder liner.

In this research, a wearable exoskeleton arm, ZJUESA, based on man-machine system is designed and a hierarchically distributed teleoperation control system is explained. This system includes three main levels: supervisor giving the command through the exoskeleton arm in safe zone with the operator interface; slave-robot working in hazardous zone; data transmission between supervisor-master and master-slave through the Internet or Ethernet. In Section 2, by using the orthogonal experiment design method, the design foundation of ZJUESA and its optimal, we hybrid fuzzy control system for the force feedback on ZJUESA. Consequently, the force feedback control simulations and experiment results analysis are presented in Section 4 [13–17].

2 Prediction Method

In order to improve the tribological performance of piston-cylinder liner system, the cylinder liner surface is usually machined by plateau honing and laser honing to form cross-hatched lines, micro dimples and grooves, as shown in Figure 1.

A method is proposed to characterize 3D roughness of textured liner processed by plateau honing, the proposed method includes the following steps: (1) Honing experiment of cylinder liner are conducted and gray image of the textured liner surface is acquired. (2) The image reference plane is reconstructed (middle and low frequency information related to waviness, shape and position error), and high frequency information of the image related to the roughness is separated accurately and the characteristic parameters of high frequency information are extracted. (3) The relationship between the characteristic parameters of high frequency information and 3D roughness is modeled to implement machine vision perception of 3D roughness. Figure 2 shows technical route of perception and evaluation of surface roughness of textured cylinder liner.

2.1 Reconstruction of Reference Plane
2.1.1 Model of Reference Plane
Figure 3 shows the gray image as well as the gray value. It is assumed that the evaluation area of 3D roughness is rectangular:

$$D = \left\{ (x,y) | x \in (a_x, b_x), y \in (c_y, d_y) \right\}, \tag{1}$$

where D is roughness evaluation area, x is the axis coordinate and y is the circumferential coordinate of evaluation area, a_x is the lower limit and b_x is the upper limit in the x direction, c_y is the lower limit and d_y is the upper limit in the y direction.

The profile characteristics of the cross-hatched liner surface are superposition of roughness, surface waviness and geometric profile and position error, etc. Therefore, the gray image can be represented in frequency domain as a superposition of high frequency information related to roughness characteristics, the middle frequency information related to surface waviness, low frequency information related to geometric shape and position error, and image noise pollution caused by light, etc.
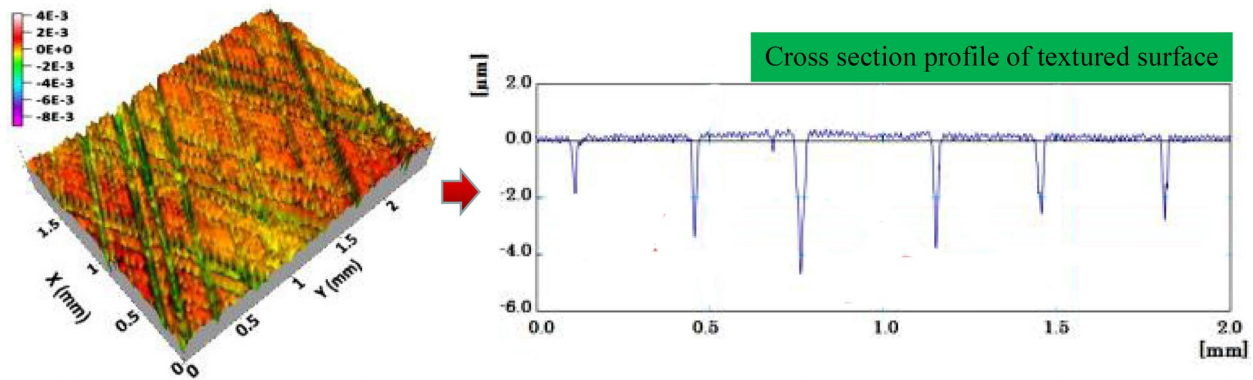
Figure 1 Micro morphology of textured cylinder liner surface

The gray matrix of the gray image can be expressed as:

$$Z = R + G + K + L, \tag{2}$$

where R is the gray matrix of high frequency image, G is the gray matrix of middle frequency image, K is the gray matrix of low frequency image, L is the gray matrix of noise caused by light, and Z is the gray matrix of liner surface image.

It is important to determine the reference plane when measuring the surface roughness. Reference plane is defined as the superposition of surface waviness and geometric profile and position error. Similarly, the reference plane of gray image can be represented as superposition of middle frequency image information and low frequency image information. The gray matrix of the reference plane can be expressed as:

$$S = G + K. \tag{3}$$

The gray matrix of high frequency image related to roughness can be represented as:

$$R = Z - S - L. \tag{4}$$

In Eq. (4), it is necessary to obtain the gray matrix of high frequency image to implement perception of 3D roughness of the cross-hatched surface, so the gray matrix of the reference plane need to be calculated when eliminating light noise of image.

2.1.2 Textured Surface Image Denoising

The light noise is low frequency component when acquiring gray image. A Butterworth high-pass filter is used to convolve the gray image to eliminate the light noise. Figure 4 shows the gray image of the cross-hatched liner surface before and after Butterworth high-pass filtering. It can be seen that light noise of the gray image is eliminated and the details are also enhanced after Butterworth high-pass filtering.

2.1.3 Reconstruction Method of Reference Plane

The reference plane of the gray image should be reconstructed to extract high frequency image information of 3D roughness. The reference plane of roughness evaluation is reconstructed usually by Gaussian filtering. However, anti-friction texture often exists on the surface of cylinder liner (such as cross-hatched lines, micro dimples and grooves), Gaussian filtering method often be lowered by the "valley" and causes distortion boundary of the reference plane. The L_∞ regression algorithm is robust and can suppress the influence of abnormal points effectively. Therefore, the L_∞ regression robust algorithm and LM algorithm are employed to construct a fitting method to reconstruct the reference plane of gray image.

The gray value of middle frequency image related to waviness can be expressed in Fourier series when surface waviness exhibits a periodic change. The variation of the geometric profile and position error meets spline function. Therefore, the gray value of low frequency image can be represented as quadratic spline function:

$$g_{i,j} = \sum_{d=1}^{k} \left[A_d \sin\left(\frac{2\pi}{\lambda_{xd}} x_i + \frac{2\pi}{\lambda_{yd}} y_j \right) + B_d \cos\left(\frac{2\pi}{\lambda_{xd}} x_i + \frac{2\pi}{\lambda_{yd}} y_j \right) \right], \tag{5}$$

$$k_{i,j} = b_0 + b_1 x_i + b_2 y_j + b_3 x_i y_j + b_4 x_i^2 + b_5 y_j^2, \tag{6}$$

where A_d is the magnitude of sine function, B_d is the magnitude of cosine function, λ_{xd} is the wavelength component in the x direction, λ_{yd} is the wavelength component in the y direction, x_i is the coordinate of pixel i in the
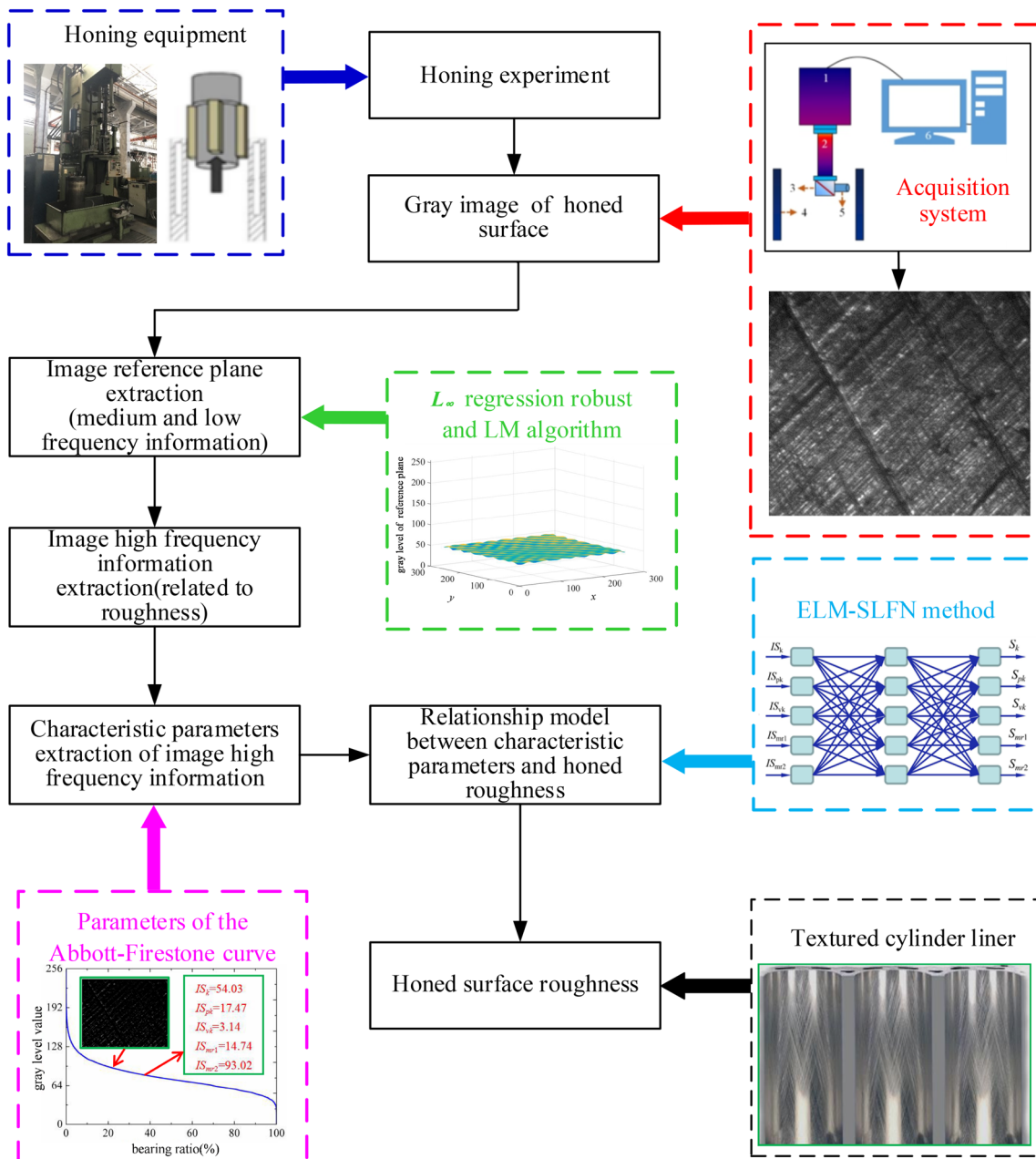
Figure 2 Technical route of perception and evaluation of surface roughness of textured cylinder liner

x direction, y_j is the coordinate of pixel i in the y direction, k is the number of sine and cosine functions, b_0– b_5 are the coefficients of the quadratic spline function.

According to the gray values of middle frequency image and low frequency image, the gray values of the reference plane can be expressed as:

$$s_{i,j} = g_{i,j} + k_{i,j}. \tag{7}$$

The gray matrix can be written in the following form:
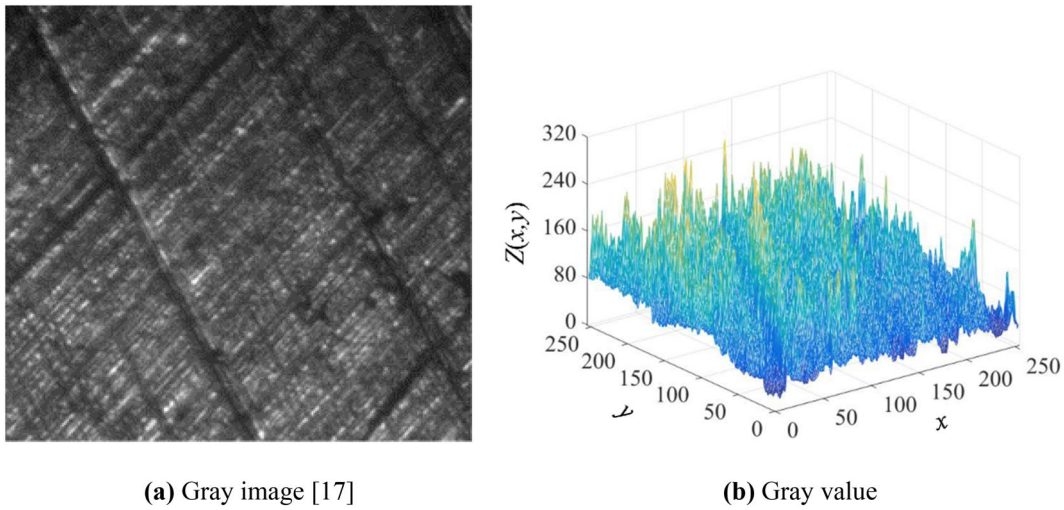
$$S_{LS} = JF_{LS}, \tag{8}$$

(a) Gray image [17]   **(b)** Gray value

Figure 3 Gray image of the cross-hatched liner surface and its gray value

(a) Gray image before filtering   **(b)** Gray image after filtering
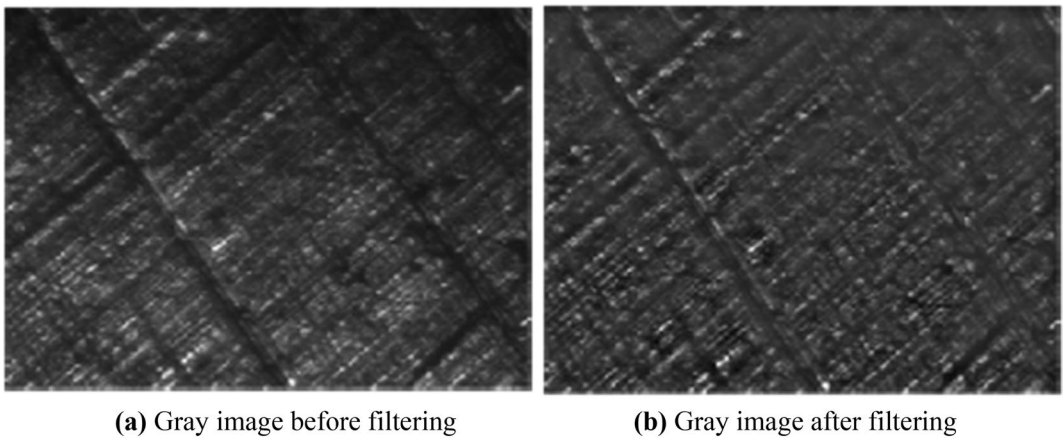
Figure 4 Gray image of cross-hatched liner surface before and after Butterworth high-pass filtering

where S_{LS} is the column vector form of the gray matrix of the reference plane, J is the Jacobian matrix of the reference plane, F_{LS} is the coefficient vector of the reference plane.

In Eq. (8), the coefficient vector, Jacobian matrix and the column vector of the gray matrix of the reference plane can be expressed as follows:

$$J = [J_1 \quad J_2], \tag{9}$$

$$F_{LS}^{\mathrm{T}} = \{b_0, b_1, \cdots, b_5, A_1, A_2, \cdots, A_k, B_1, B_2, \cdots, B_k\}, \tag{10}$$

$$S_{LS}^{\mathrm{T}} = \{s_{1,1}, s_{1,2}, \cdots, s_{1,n}, \cdots, s_{j,1}, s_{j,2},$$
$$\cdots, s_{j,n}, \cdots, s_{m,1}, s_{m,2}, \cdots, s_{m,n}\}, \tag{11}$$

$$J_1 = \begin{bmatrix} 1 & x_1 & y_1 & x_1y_1 & x_1^2 & y_1^2 \\ 1 & x_1 & y_2 & x_1y_2 & x_1^2 & y_2^2 \\ \vdots & \vdots & \vdots & \vdots & \vdots & \vdots \\ 1 & x_1 & y_n & x_1y_n & x_1^2 & y_n^2 \\ 1 & x_2 & y_1 & x_2y_1 & x_2^2 & y_1^2 \\ 1 & x_2 & y_2 & x_2y_2 & x_2^2 & y_2^2 \\ \vdots & \vdots & \vdots & \vdots & \vdots & \vdots \\ 1 & x_2 & y_n & x_2y_n & x_2^2 & y_n^2 \\ \vdots & \vdots & \vdots & \vdots & \vdots & \vdots \\ 1 & x_m & y_1 & x_my_1 & x_m^2 & y_1^2 \\ 1 & x_m & y_2 & x_my_2 & x_m^2 & y_2^2 \\ \vdots & \vdots & \vdots & \vdots & \vdots & \vdots \\ 1 & x_m & y_n & x_my_n & x_m^2 & y_n^2 \end{bmatrix}, \tag{12}$$

$$J_2 = \begin{bmatrix} \sin(w_{x1}x_1 + w_{y1}y_1) & \cdots & \sin(w_{xk}x_1 + w_{yk}y_1) & \cos(w_{x1}x_1 + w_{y1}y_1) & \cdots & \cos(w_{xk}x_1 + w_{yk}y_1) \\ \sin(w_{x1}x_1 + w_{y1}y_2) & \cdots & \sin(w_{xk}x_1 + w_{yk}y_2) & \cos(w_{x1}x_1 + w_{y1}y_2) & \cdots & \cos(w_{xk}x_1 + w_{yk}y_2) \\ \vdots & \vdots & \vdots & \vdots & \vdots & \vdots \\ \sin(w_{x1}x_1 + w_{y1}y_n) & \cdots & \sin(w_{xk}x_1 + w_{yk}y_n) & \cos(w_{x1}x_1 + w_{y1}y_n) & \cdots & \cos(w_{xk}x_1 + w_{yk}y_n) \\ \sin(w_{x1}x_2 + w_{y1}y_1) & \cdots & \sin(w_{xk}x_2 + w_{yk}y_1) & \cos(w_{x1}x_2 + w_{y1}y_1) & \cdots & \cos(w_{xk}x_2 + w_{yk}y_1) \\ \sin(w_{x1}x_2 + w_{y1}y_2) & \cdots & \sin(w_{xk}x_2 + w_{yk}y_2) & \cos(w_{x1}x_2 + w_{y1}y_2) & \cdots & \cos(w_{xk}x_2 + w_{yk}y_2) \\ \vdots & \vdots & \vdots & \vdots & \vdots & \vdots \\ \sin(w_{x1}x_2 + w_{y1}y_n) & \cdots & \sin(w_{xk}x_2 + w_{yk}y_n) & \cos(w_{x1}x_2 + w_{y1}y_n) & \cdots & \cos(w_{k}x_2 + w_{yk}y_n) \\ \vdots & \vdots & \vdots & \vdots & \vdots & \vdots \\ \sin(w_{x1}x_m + w_{y1}y_1) & \cdots & \sin(w_{xk}x_m + w_{yk}y_1) & \cos(w_{x1}x_m + w_{y1}y_1) & \cdots & \cos(w_{xk}x_m + w_{yk}y_1) \\ \sin(w_{x1}x_m + w_{y1}y_2) & \cdots & \sin(w_{xk}x_m + w_{yk}y_2) & \cos(w_{x1}x_m + w_{y1}y_2) & \cdots & \cos(w_{xk}x_m + w_{yk}y_2) \\ \vdots & \vdots & \vdots & \vdots & \vdots & \vdots \\ \sin(w_{x1}x_m + w_{y1}y_n) & \cdots & \sin(w_{xk}x_m + w_{yk}y_n) & \cos(w_{x1}x_m + w_{y}y_n) & \cdots & \cos(w_{xk}x_m + w_{yk}y_n) \end{bmatrix}. \tag{13}$$

The gray matrix can be calculated by L∞ regression robust algorithm and LM algorithm. The calculation process of gray matrix is shown in Figure 5. The coefficient vector of the gray image reference plane can be expressed as:

$$F_{LS} = \left(J^\mathrm{T} J\right)^{-1} J^\mathrm{T} S_{LS}. \tag{14}$$

In order to minimize the maximum residual error required by L∞ regression robust algorithm, according to L∞ regression criterion, the gray matrix can be written as:

$$\|Z - JF_{LS}\|_\infty \to \min, \tag{15}$$

$$Z = JF_{LS} + R, \tag{16}$$

$$R = R_1 f, \tag{17}$$

$$R_1 = \{|r_{1,1}|, \cdots, |r_{1,n}|, \cdots, |r_{j,1}|, \cdots, |r_{j,n}|, \cdots, \\ |r_{m,1}|, \cdots, |r_{m,n}|\}^\mathrm{T}, \tag{18}$$

$$f = \{f_{1,1}, \cdots, f_{1,n}, \cdots, f_{j,1}, \cdots, f_{j,n}, \cdots, f_{m,1}, \cdots f_{m,n}\}, \tag{19}$$

where R is the residual error vector of the image reference plane, $r_{i,j}$ is the residual value of the gray level of the reference plane, $f_{i,j}$ is the transform coefficient which is 1 when the residual value is non-negative, otherwise is -1.

According to the L_∞ regression, the optimum solution of the coefficient vector of the reference plane of gray image can be expressed as:

$$Z^* = JF_{LS}^* + fR^*, \tag{20}$$

where F_{LS}^* is the optimum solution of the coefficient vector, Z^* is the gray image matrix of optimum solution, R^* is the residual vector of optimum solution.

In order to obtain the optimum solution of the coefficient vector and eliminate the residual, LM algorithm is used to iterate the residual vector and form a modified vector of the coefficient vector. According to LM algorithm, the optimum solution of the coefficient vector can be expressed as [25, 26]:

$$F_{LS}^* = F_{LS} + \Delta F \tag{21}$$

with

$$\Delta F = \left(J^\mathrm{T} J + \mu I\right)^{-1} J^\mathrm{T} R, \tag{22}$$

where μ is the damping factor, I is the identity matrix, ΔF is the modification vector.

2.2 Extraction of High Frequency Characteristics and Roughness Prediction

2.2.1 Extraction Method

Based on reconstruction of the reference plane of the gray image, high frequency gray image information of 3D roughness characteristics can be acquired according to Eq. (5). Abbott-Firestone curve [27] is often used to characterize the roughness characteristics of the actual profile. Therefore, Abbott-Firestone curve is used to describe high frequency gray image information. According to the definition of Abbott-Firestone curve, high frequency gray image information can be characterized by the following parameters: core roughness depth (Sk), reduced peak height (Spk), reduced valley depth (Svk), bearing length ratios (Smr1, Smr2). Figure 6 shows the parameters of Abbott-Firestone curve for high frequency gray image.
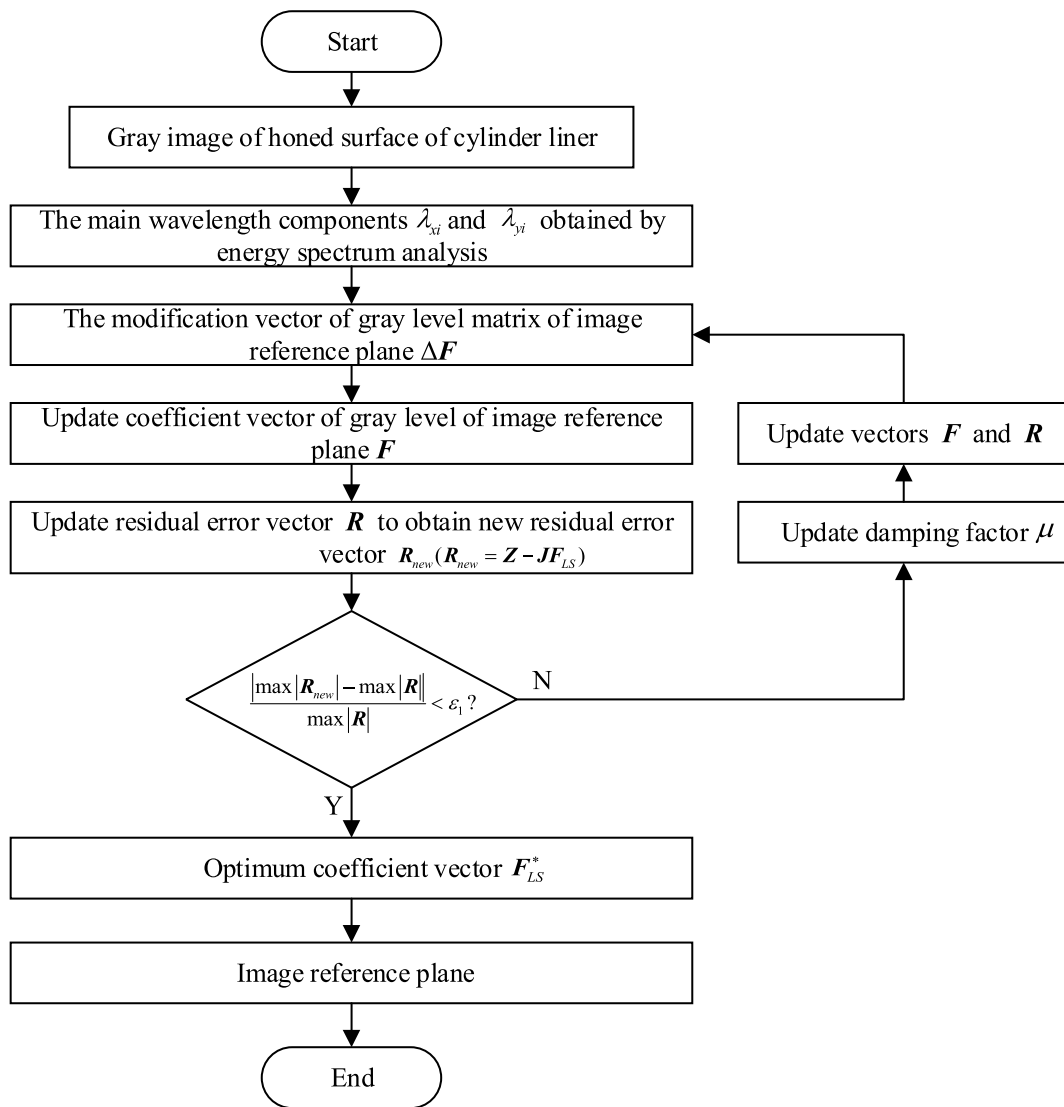
```
                              ┌──────────┐
                              │  Start   │
                              └────┬─────┘
                                   ▼
            ┌──────────────────────────────────────────────┐
            │  Gray image of honed surface of cylinder liner │
            └───────────────────┬──────────────────────────┘
                                ▼
        ┌────────────────────────────────────────────────────┐
        │ The main wavelength components λxi and λyi obtained by│
        │            energy spectrum analysis                  │
        └───────────────────────┬────────────────────────────┘
                                ▼
      ┌──────────────────────────────────────────────────────┐     ┌──────────────────────┐
      │ The modification vector of gray level matrix of image │◄────│ Update vectors F and R│
      │          reference plane ΔF                           │     └──────────┬───────────┘
      └───────────────────────┬──────────────────────────────┘                │
                              ▼                                                │
      ┌──────────────────────────────────────────────────────┐     ┌──────────────────────┐
      │ Update coefficient vector of gray level of image reference│  │ Update damping factor μ│
      │             plane F                                   │     └──────────┬───────────┘
      └───────────────────────┬──────────────────────────────┘                │
                              ▼                                                │
      ┌──────────────────────────────────────────────────────┐                │
      │ Update residual error vector R to obtain new residual error│            │
      │      vector Rnew (Rnew = Z − JFLS)                    │                │
      └───────────────────────┬──────────────────────────────┘                │
                              ▼                                                │
                        ◇ condition ◇ ── N ──────────────────────────────────┘
                              │ Y
                              ▼
```

Figure flow chart nodes:

- Start
- Gray image of honed surface of cylinder liner
- The main wavelength components λ_{xi} and λ_{yi} obtained by energy spectrum analysis
- The modification vector of gray level matrix of image reference plane ΔF
- Update coefficient vector of gray level of image reference plane F
- Update residual error vector R to obtain new residual error vector R_{new} ($R_{new} = Z - JF_{LS}$)
- Decision: $\dfrac{\left|\max|R_{new}| - \max|R|\right|}{\max|R|} < \varepsilon_1 ?$ — N → Update damping factor μ → Update vectors F and R
- Y → Optimum coefficient vector F_{LS}^{*}
- Image reference plane
- End

Figure 5 Calculation flow chart of the reference plane of gray image
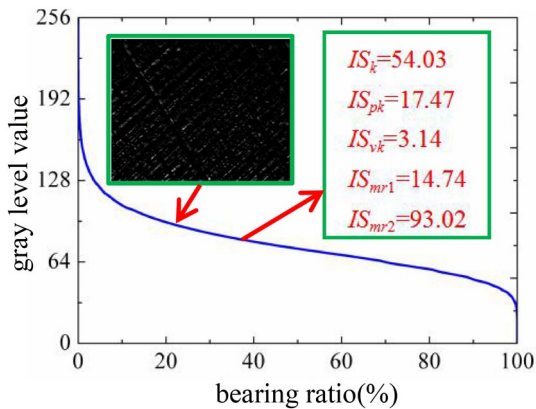
Figure 6 Parameters of Abbott-Firestone curve for high frequency gray image

Plot labels: gray level value vs bearing ratio(%)

$IS_k = 54.03$
$IS_{pk} = 17.47$
$IS_{vk} = 3.14$
$IS_{mr1} = 14.74$
$IS_{mr2} = 93.02$

2.2.2 Roughness Characteristics Prediction Method

Based on the extreme learning machine, single-hidden layer feedforward neural network (i.e., ELM-SLFN method) is used to model the relationship between Abbott-Firestone curve and 3D roughness (i.e., characteristic parameters of Abbott-Firestone curve of the actual profile). The model is used to predict 3D roughness. Figure 7 shows the schematic diagram of ELM-SLFN model. The input layer (input: Abbott-Firestone curve characteristic parameters of high frequency gray image), hidden layer and output layer (output: Abbott-Firestone curve characteristic parameters of measured rough profile) neurons of ELM-SLFN model use a fully connected mode to transfer data. The ELM is used to
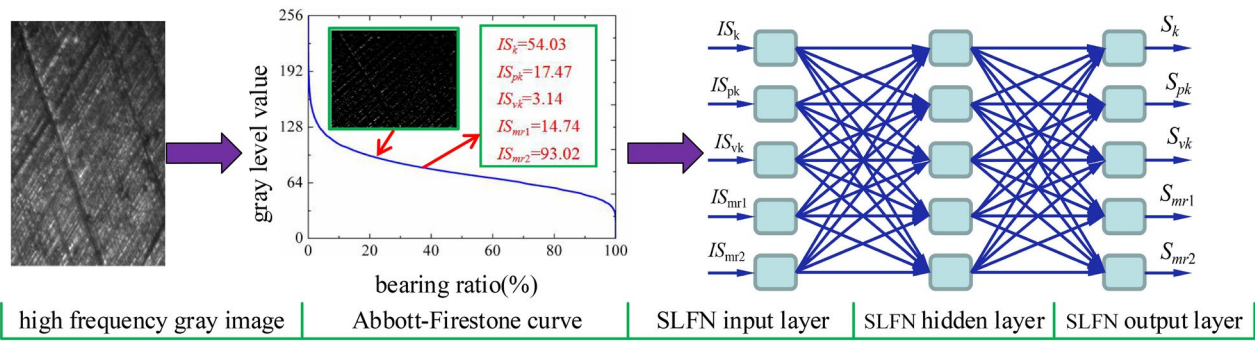
Figure 7 ELM-SLFN model for the prediction of 3D roughness

obtain the connection weight matrix and the threshold vector [28].

3 Results and Discussion

3.1 Acquisition System of Gray Image

The cross-hatched surface of liner is honed on a honing machine. The honing machine and cross-hatched surface of liner is shown in Figure 8. Figure 9 shows the honing process of cross-hatched surface of liner. The gray image acquisition system is shown in Figure 10, which includes CCD industrial camera, eyepiece, objective lens, image processor and display device, etc. The performance indexes of each device are: the resolution of CCD is 1920×1080 pixels, the magnification of eyepiece and objective lens is 0.5× and 4.0× respectively, the main frequency and memory of the image processor are 3.1 Hz and 8.0 GB respectively, and the resolution of the image display is 1920×1080 pixels. It should be noted that the image acquired by CCD is a color image of RGB (i.e., red, green and blue) three-channel, which can be converted to gray image using the color space conversion algorithm recommended by Adobe Photoshop.
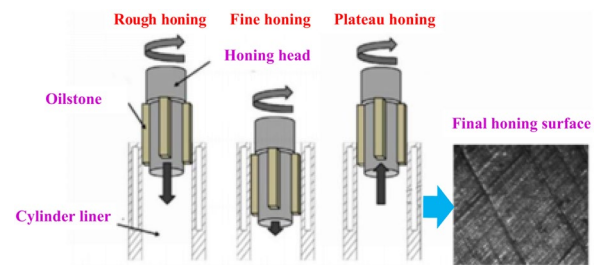
Figure 9 Honing process of cross-hatched surface of liner

1 — CCD industrial camera
2 — eyepiece
3 — 45 degree mirror
4 — cylinder liner
5 — objective lense
6 — image processor
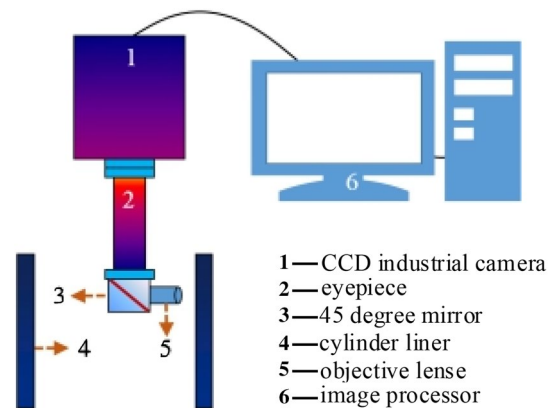
Figure 10 Schematic diagram of acquisition system of gray image
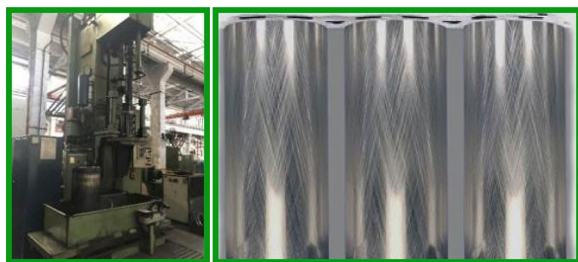
Figure 8 The honing machine and cross-hatched surface of liner

3.2 Validation of Reconstruction of Image Reference Plane

In order to verify the effectiveness of L∞ regression robust algorithm and LM algorithm to reconstruct the reference plane of gray image, based on the gray image shown in Figure 4, the reference plane is reconstructed by L_∞ and LM algorithms and Gaussian quadratic filtering method (ISO13565-1 recommended method) respectively as shown in Figure 11. It can be seen that gray level of reference plane reconstructed by Gaussian quadratic
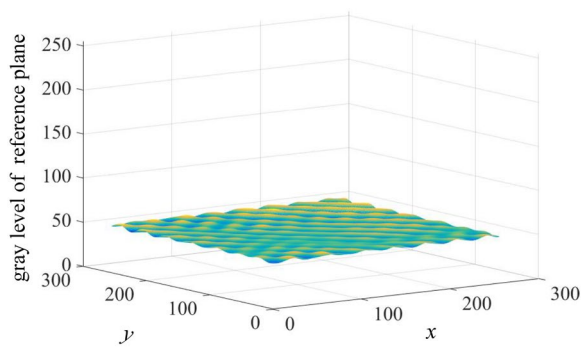
(a) L∞ regression robust and LM algorithms
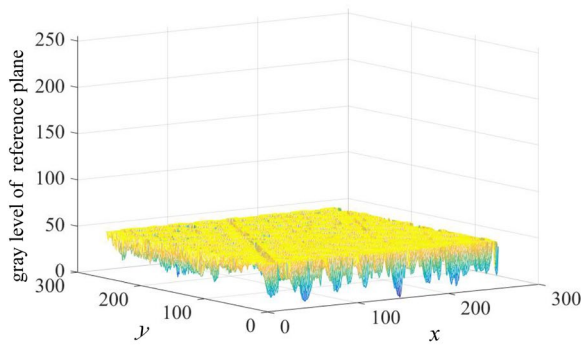
(b) Gaussian quadratic filtering method

Figure 11 Reference plane of gray image of cross-hatched liner surface solved by different methods

filtering method fluctuates greatly, and the reference plane leaves a "dent" on the cross-hatched liner and boundary of the evaluation area. Compared with Gaussian quadratic filtering method, L_∞ and LM algorithms are less affected by the cross-hatched lines and boundary of the evaluation area, and fluctuation is smaller. This indicates that L_∞ and LM algorithms can effectively avoid the influence of boundary distortion and abnormal points when reconstruct the gray image reference plane.

3.2.1 Extraction of High Frequency Image Features
In order to study correlation of the parameters of Abbott-Firestone curve and the parameters (3D roughness characteristics) obtained from the measured profile, the parameters of Abbott-Firestone curve of the actual rough profile are measured using the confocal microscope. Figures 12 and 13 show correlation of calculated parameters of Abbott-Firestone curve and 3D roughness

characteristics. It can be seen that there is a strong correlation of parameters of Abbott-Firestone curves between gray image and the measured profile. The bearing length ratios high frequency gray image and measured bearing length ratios have the same change trend. The Spk, Sk, and Svk of the high frequency gray image and the measured profile have the opposite trend.

3.2.2 Validation of Roughness Prediction
In order to implement machine vision perception and prediction of 3D roughness characteristics of cross-hatched liner surface of cylinder liner, 28 sets of honing experiments are conducted to acquire the gray images of cross-hatched surface of liner. On this basis, the characteristic parameters of Abbott-Firestone curve can be calculated. 3D roughness of actual profile is measured by a confocal microscope. The parameters of Abbott-Firestone curve are shown in Figure 12. The characteristic parameters of Abbott-Firestone curve of both high frequency gray image and measured profile are used as training samples (24 sets) to construct ELM-SLFN model for 3D roughness prediction. Another four groups I, Z, K and L shown in Figures 12 and 13 are used as the test samples to verify the effectiveness of ELM-SLFN prediction model. Table 1 shows 3D roughness characteristics of actual profile predicted by ELM-SLFN model and the parameters of Abbott-Firestone curve of the measured profile. The relative error between the predicted and measured parameters of Abbott-Firestone curve is shown in Table 2, it can be seen that the predicted parameters are in good agreement with the measured parameters. The relative error remains in the range of 2.0%–8.5%. The results show that ELM-SLFN model can effectively predict 3D roughness characteristics of cross-hatched surface of liner.

4 Conclusions
L_∞ regression robust and LM algorithms are employed to reconstruct the gray image reference plane of cross-hatched surface of cylinder liner. The roughness characteristics of high frequency gray image are separated, and the parameters of Abbott-Firestone curve are extracted. On this basis, ELM-SLFN method is proposed to establish prediction model of relationship of parameters of Abbott-Firestone curve and 3D roughness. The machine vision perception and evaluation of 3D roughness characteristics can be implemented.
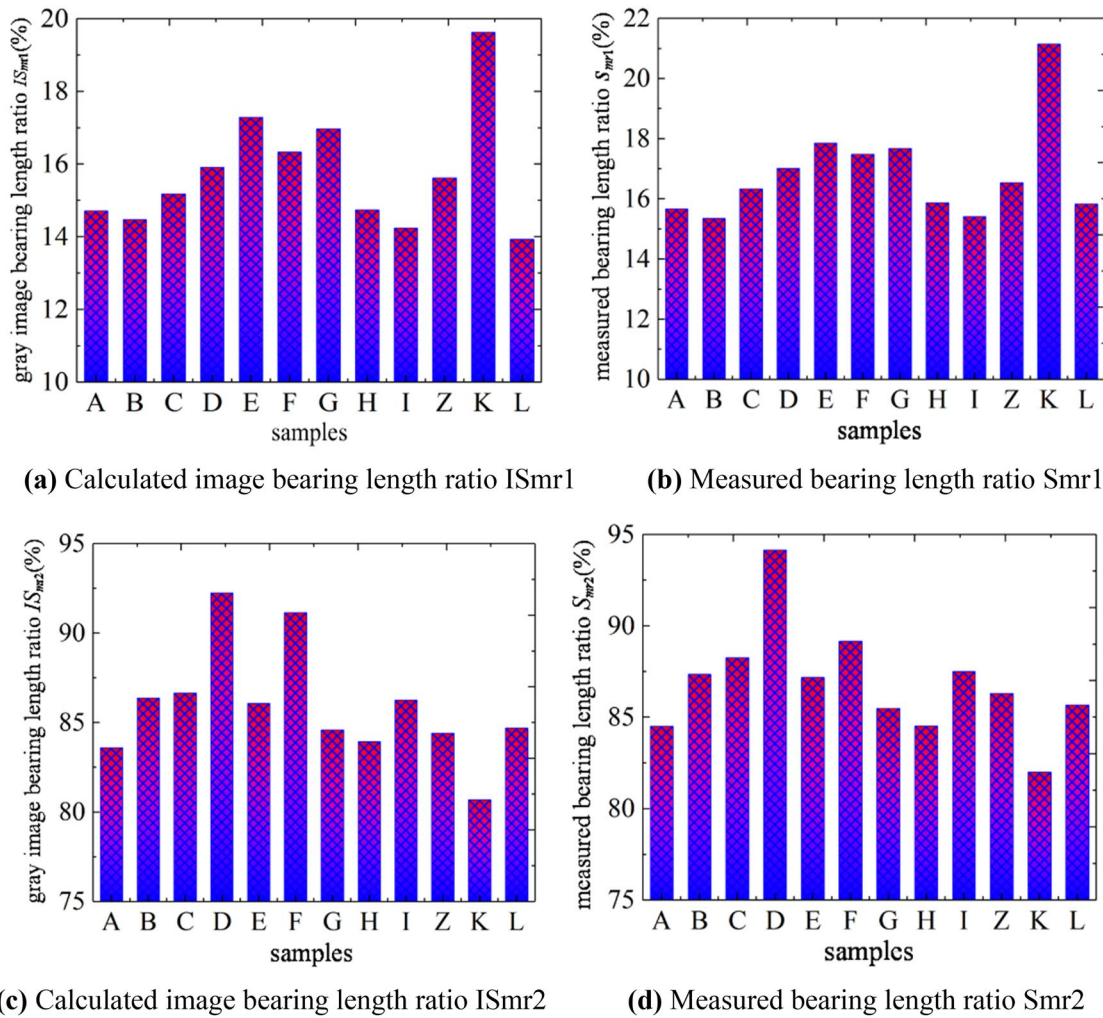
(a) Calculated image bearing length ratio ISmr1

(b) Measured bearing length ratio Smr1

(c) Calculated image bearing length ratio ISmr2

(d) Measured bearing length ratio Smr2

Figure 12 Parameters of Abbott-Firestone curve of the high frequency gray image and measured profile with same change trend

(1) Comparing with Gaussian quadratic filtering method, L∞ regression robust and LM algorithms can effectively reconstruct the reference plane of gray image, and can avoid the influence of boundary distortion and abnormal points.

(2) Comparing with the change of parameters of Abbott-Firestone curve of gray image and the measured profile, the results indicate that it is feasible to use Abbott-Firestone curve parameters of high fre-quency gray images to characterize 3D roughness characteristics.

(3) Comparing the predicted parameters of Abbott-Firestone curve with measured, the results show that ELM-SLFN model can effectively predict 3D roughness, and the relative error remains in the range of 2.0%–8.5%.
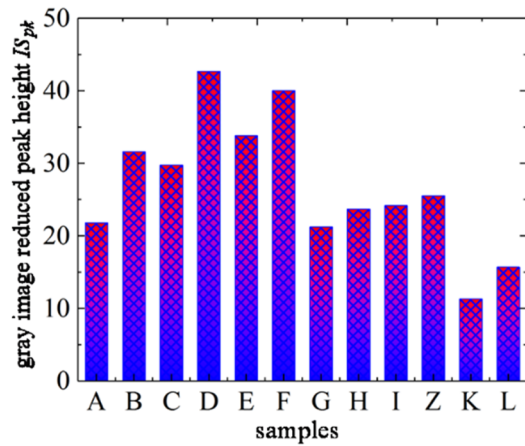
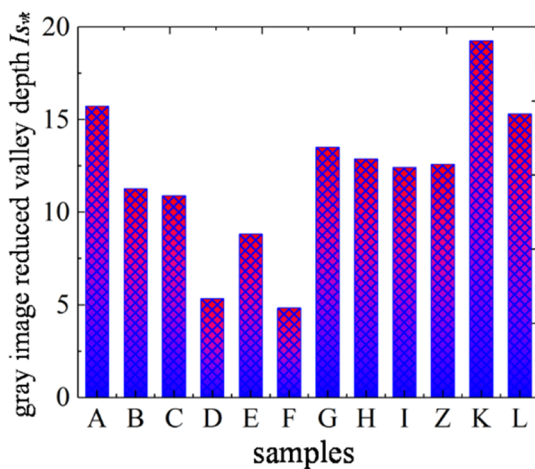**(a)** Calculated image reduced peak height ISpk
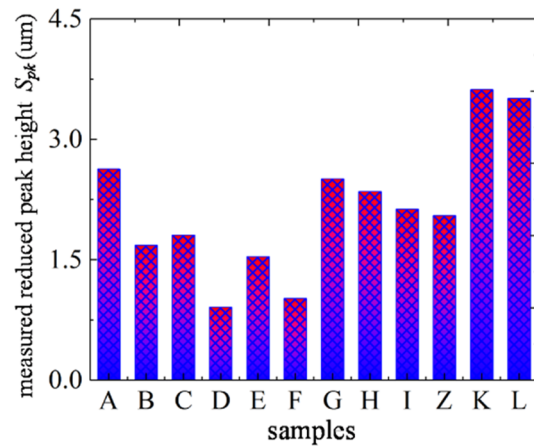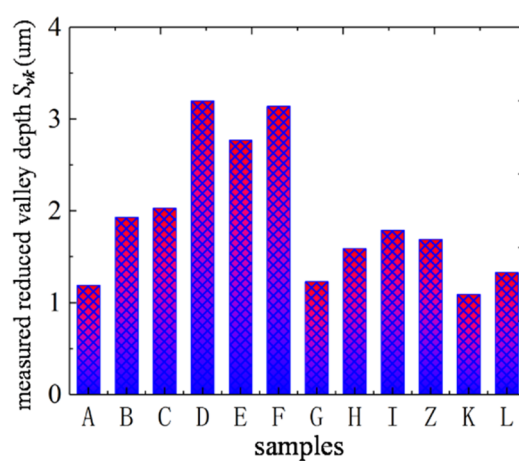

(b) Measured reduced peak height Spk
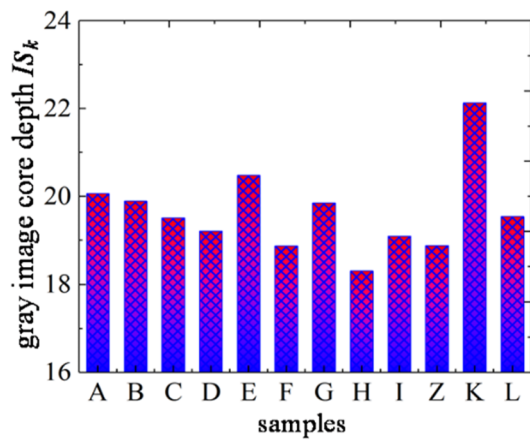
(c) Calculated image core depth ISk
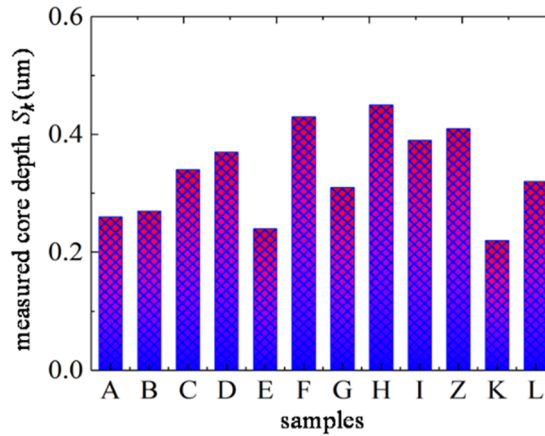
(d) Measured core depth Sk

(e) Calculated image reduced valley depth ISvk

(f) Measured reduced valley depth Svk

Figure 13 Parameters of Abbott-Firestone curve of the high frequency gray image and measured profile with opposite change trend

Table 1 The predicted and measured parameters of Abbott-Firestone curves

Parameters	Sample I		Sample Z		Sample K		Sample L	
	Predicted	**Measured**	**Predicted**	**Measured**	**Predicted**	**Measured**	**Predicted**	**Measured**
S_{mr1} (%)	14.76	15.41	17.07	16.54	21.61	21.15	16.49	15.83
S_{mr2} (%)	91.93	87.50	82.51	86.31	76.74	81.99	90.21	85.67
S_{pk} (µm)	2.06	2.13	2.10	2.05	3.75	3.62	3.22	3.51
S_k (µm)	0.42	0.39	0.43	0.41	0.23	0.22	0.33	0.32
S_{vk} (µm)	1.87	1.79	1.58	1.69	1.01	1.09	1.37	1.33

Table 2 The relative error between the predicted and measured parameters of Abbott-Firestone curves

Parameters	Sample I Prediction error (%)	Sample Z Prediction error (%)	Sample K Prediction error (%)	Sample L Prediction error (%)
S_{mr1}	4.2	3.2	2.2	4.2
S_{mr2}	5.1	4.4	6.4	5.3
S_{pk}	3.3	2.4	3.6	8.3
S_k	7.7	4.8	4.5	3.1
S_{vk}	4.5	6.5	7.3	3.0

Declarations

Competing Interests
The authors declare no competing interests.

References
[1] R Keribar, Z Dursunkaya, M F Flemming. An integrate model of ring pack performance. *Journal of Engineering for Gas Turbines and Power*, 1991, 113(3): 382-389.
[2] A Irimescu, C Tornatore, L Marchitto, et al. Compression ratio and blow-by rates estimation based on motored pressure trace analysis for an optical spark ignition engine. *Applied Thermal Engineering*, 2013, 61(2): 101-109.
[3] J Sun, X Huang, G S Liu, et al. Research on the status of lubricating oil transport in piston skirt-cylinder liner of engine. *Journal of Tribology*, 2018, 140(4): 041702.
[4] C M Taylor. Automobile engine tribology—design considerations for efficiency and durability, *Wear*, 1998, 221(1): 1-8.
[5] T Grosse, M Winter, S Baron, et al. Honing with polymer based cutting fluids. *CIRP Journal of Manufacturing Science and Technology*, 2015, 11: 89-98.
[6] R A Mezari, R S F Pereira, F J P Sousa, et al. Wear mechanism and morphologic space in ceramic honing process. *Wear*, 2016, 362: 33-38.
[7] B Goeldel, M E Mansori, D Dumur. Macroscopic simulation of the liner honing process. *CIRP Annals*, 2012, 61(1): 319-322.
[8] F Cabanettes, Z Dimkovski, B-G Rosén. Roughness variations in cylinder liners induced by honing tools' wear. *Precision Engineering*, 2015, 41: 40-46.
[9] I B Corral, J V Calvet, M C Salcedo. Modelling of surface finish and material removal rate in rough honing. *Precision Engineering*, 2014, 38(1): 100-108.
[10] J J Liu, Y J Jiang, D S Grierson, et al. Tribochemical wear of diamond-like carbon-coated atomic force microscope tips. *ACS Applied Materials & Interfaces*, 2017, 9(40): 35341-35348.
[11] Y Wang, E I Meletis, H Huang. Quantitative study of surface roughness evolution during low-cycle fatigue of 316L stainless steel using Scanning Whitelight Interferometric (SWLI) Microscopy. *International Journal of Fatigue*, 2013, 48: 280-288.
[12] X H Zhang, Y Xu, R L Jackson. An analysis of generated fractal and measured rough surfaces in regards to their multi-scale structure and fractal dimension. *Tribology International*, 2017, 105: 94-101.
[13] M Papanikolaou, K Salonitis. Fractal roughness effects on nanoscale grinding. *Applied Surface Science*, 2019, 467: 309-319.
[14] L S Matthew. Zappulla, S M Cho, et al. Multiphysics modeling of continuous casting of stainless steel. *Journal of Materials Processing Technology*, 2019, 278: 116469.
[15] E H Lu, R T Zhang, J Liu, et al. Observation of ground surface roughness values obtained by stylus profilometer and white light interferometer for common metal materials. *Surface and Interface Analysis*, 2022, 54(6): 587-599.
[16] H F Tao, Y H Liu, D W Zhao, et al. Undeformed chip width non-uniformity modeling and surface roughness prediction in wafer self-rotational grinding process. *Tribology International*, 2022, 171: 107547.

[17] K D Lawrence, R Shanmugamani, B Ramamoorthy. Evaluation of image based Abbott–Firestone curve parameters using machine vision for the characterization of cylinder liner surface topography. *Measurement*, 2014, 55: 318-334.

[18] G Samtas. Measurement and evaluation of surface roughness based on optic system using image processing and artificial neural network. *The International Journal of Advanced Manufacturing Technology*, 2014, 73(1): 353-364.

[19] U Zuperl, F Cus. Surface roughness fuzzy inference system within the control simulation of end milling. *Precision Engineering*, 2016, 43: 530-543.

[20] H A Yi, J Liu, E H Lu, et al. Measuring grinding surface roughness based on the sharpness evaluation of colour images. *Measurement Science and Technology*, 2016, 27(2): 1-14.

[21] J Liu, E H Lu, H A Yi, et al. A new surface roughness measurement method based on a color distribution statistical matrix. *Measurement*, 2017, 103: 165-178.

[22] X J Zhao, H A Yi, Y L Chen, et al. Devwelopment and evaluation of a color-image-based visual roughness measurement method with illumination robustness. *Journal of the Optical Society of America A*, 2021, 38(3): 369-377.

[23] E H Lu, J Liu, R Y Gao, et al. Designing indices to measure surface roughness based on the color distribution statistical matrix (CDSM). *Tribology International*, 2018, 122: 96-107.

[24] R S Umamaheswara Raju, V Ramachandra Raju, R Ramesh. Curvelet transform for estimation of machining performance. *Optik*, 2017, 131: 615-625.

[25] A A Jebur, W Atherton, M A Khaddar, et al. Performance analysis of an evolutionary LM algorithm to model the load-settlement response of steel piles embedded in sandy soil. *Measurement*, 2019, 140: 622-635.

[26] D S Gonçalves, M L N Gonçalves, F R Oliveira. An inexact projected LM type algorithm for solving convex constrained nonlinear equations. *Journal of Computational and Applied Mathematics*, 2021, 391: 113421.

[27] V Dzyura, P Maruschak. Optimizing the formation of hydraulic cylinder surfaces, taking into account their microrelief topography analyzed during different operations. *Machines*, 2021, 9(6): 116.

[28] H Men, S L Fu, J L Yang. Comparison of SVM, RF and ELM on an electronic nose for the intelligent evaluation of paraffin samples. *Sensors*, 2018, 18(1): 285.

Yanjun Lü male, born in 1972, is currently a professor at *School of Mechanical and Precision Instrument Engineering, Xi'an University of Technology, China*. His research interests include industrial lubrication and engineering tribology, design science and intelligent manufacturing, nonlinear dynamics and control.

Cheng Liu male, born in 1988. He received his PhD degree from *Xi'an University of Technology, China in 2020*. His research interests include hydrodynamic lubrication of the surface texture, rough surface topography characterization.

Yongfang Zhang female, born in 1975, is currently a professor at *School of Printing, Packaging Engineering and Digital Media Technology, Xi'an University of Technology, China*. Her research interests include industrial lubrication and engineering tribology, printing, packaging equipment and intelligent manufacturing.

Cheng Jiang male, born in 1996. He received his master degree from *Xi'an University of Technology, China* in 2022. His research interests include image inspection and evaluation of surface roughness, intelligent optimization algorithm.

Xudong Bai male, born in 1998, He received his master degree from *Xi'an University of Technology, China* in 2023. His research interests include dynamics of engine crankshaft system, lubrication of oil film bearing.

Zhiguo Xing male, born in 1979, is currently an associate research fellow at *National Key Laboratory for Remanufacturing, Army Academy of Armored Forces, China*. His research interests include surface tribology, performance of piezoelectric coating.